sciendo
Austrian Journal of Earth Sciences | Vienna | 2025 | Volume 118 | 157–174 | DOI: 10.17738/ajes.2025.0009

Kinematics of the Plattengneis Shear Zone, Koralpe, Eastern Alps. Constraints from Quartz Lattice Preferred Orientations

Elizabeth R. Hatley[1], Kurt Stüwe[2*], Mark A. Helper[1], William D. Carlson[1]

[1)] Department of Earth and Planetary Sciences, Jackson School of Geosciences, University of Texas at Austin, Austin, Texas, 78712, USA
[2)] University of Graz, Institute for Earth Sciences, Universitätsplatz 2, 8010 Graz, Austria
[*)] Corresponding author

Keywords: Plattengneis, electron backscatter diffraction (EBSD), quartz LPOs (lattice preferred orientations), kinematics

Abstract

Large-scale models for the tectonometamorphic evolution of the Koralpe (Eastern Alps) must account for the kinematics of deformation in the regional, intracrustal transport horizon known as the Plattengneis shear zone. Published tectonic models have invoked a range of interpretations that imply different distributions for strain geometry and shear sense, both laterally from north to south and vertically across the flat-lying shear zone. To acquire data suitable for differentiating among such models, this study presents quartz lattice preferred orientations, measured using electron backscatter diffraction, from oriented samples collected specifically to provide systematic vertical and lateral coverage of the Plattengneis shear zone. The vertical position within the shear zone is determined using a 3D model of the shear zone geometry that was made for this study in refinement of earlier work. The results yield information on activated slip systems, deformation temperatures and shear sense as a function of the vertical and lateral position within the shear zone. No systematic correlations were found between the vertical position of samples within the shear zone and their inferred sense of shear, or strain geometry. Deformation temperatures, however, display lateral distributions consistent with the regional metamorphic temperature field-gradient defined by prior petrological studies, implying that deformation of the shear zone took place predominantly at or near peak metamorphic temperatures. The observations, measurements and inferences from this study indicate that deformation of the Plattengneis occurred within the range of ~500 °C to 700 °C in an environment that has largely, but not exclusively, non-coaxial top-to-the-north shear sense. This result is consistent with recently invoked tectonic models for the shear zone.

1. Introduction

The Plattengneis is a major shear zone located in the Austroalpine system in the Eastern Alps of Austria. The shear zone ranges from 250 m to 600 m in thickness, and due to its flat-lying nature, extends over a large area of ~1000 km^2 on the eastern slopes of the Koralpe range (Fig. 1). It displays a well-developed, near-horizontal mylonitic fabric as well as a distinct north-trending stretching lineation (Krohe, 1987; Tenczer and Stüwe, 2003; Putz et al., 2006). The shear zone is developed in high grade Eoalpine metapelitic gneisses and schists and is surrounded by units of similar lithology. These pelitic to semi-pelitic units also host a series of eclogite bodies that were defined by Haüy (1822) as the eclogite type locality.

Although it is widely accepted that the Plattengneis shear zone is the largest syn-deformational structure of the early Cretaceous Eoalpine event in the Eastern Alps (e.g., Tenczer and Stüwe, 2003 and references therein), it has proven difficult to interpret its role during Eoalpine subduction. In part, this is due to the absence of distinct lithological or structural differences on either side of the flat lying shear zone, the lack of unambiguous shear

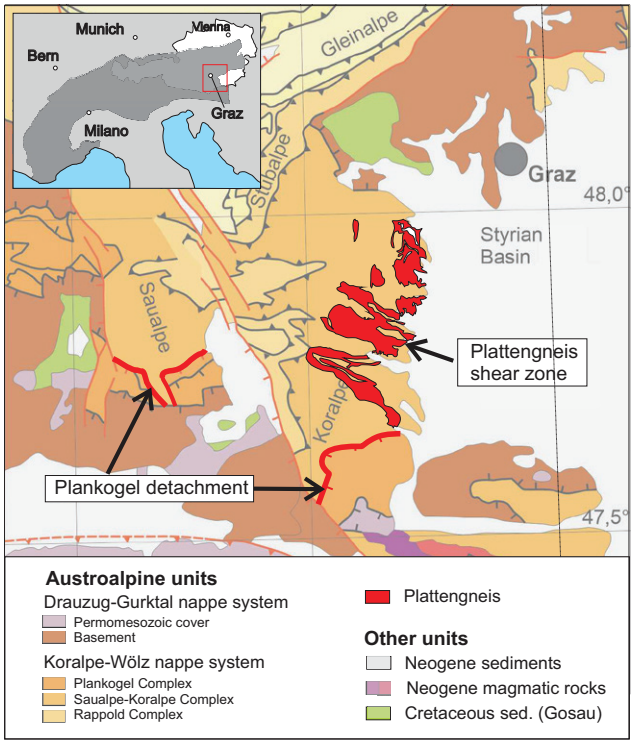

Figure 1: Geological map of the eastern end of the Alps showing various nappes of the Austroalpine nappe system (faint orange and brown tones) and the distribution of the flat-lying Plattengneis shear zone on the eastern slopes of the Koralpe range as well as the Plankogel detachment in bright red.

sense indicators, and a poorly understood 3D geometry (Kurz et al., 2002).

In this study we contribute to the understanding of the Plattengneis shear zone regarding two main aspects. Firstly, we present a series of quartz lattice preferred orientations (LPOs), measured using electron backscatter diffraction (EBSD), from well-defined locations within the shear zone (i.e. near hanging wall, near foot wall, near center etc.). Secondly, we present an updated 3D model of the shear zone (updated from Putz et al., 2006) that incorporates new field data and a higher resolution digital elevation model (DEM) to define the vertical position of our samples within the shear zone.

1.1. Previous models and working hypothesis

Previous studies include a range of petrographic data and varying interpretations of the tectonic significance of the Plattengneis within the Koralpe region. Petrologically, the general Koralpe region is well known to be of eclogite facies metamorphic grade with peak metamorphic conditions on the order of 18 kbar and 700 °C around 90–100 Ma (Thöni and Jagoutz, 1993; Miladinova et al., 2021). The metamorphic field gradient is gradational to the north (Tenczer and Stüwe, 2003) and more abrupt to the south across the Plankogel detachment showing amphibolite facies grade conditions (Herg and Stüwe, 2018). Cooling rates following the metamorphic peak were determined by Ehlers et al. (1994).

Tectonic models inferring the significance of the Plattengneis shear zone and the region were devised by Krohe (1987), Kurz et al. (2002), and Eberlei et al. (2014) and imply significantly different distributions for strain geometry and shear sense, both laterally from north to south and vertically within the shear zone (Fig. 2). The kinematic scenario advocated by Krohe (1987) implies a dominance of simple shear and a top-to-the-north shear sense throughout the shear zone (Fig. 2a). This model was substantially revised by Kurz et al. (2002), who published quartz fabric data from the shear zone and interpreted a top-to-the-north shear sense in the northern parts of the shear zone and top-to-the-south in its southern parts (Fig. 2b). Based on these observations they suggested an extensional environment in which the Plattengneis is partly responsible for the exhumation of the eclogite facies rocks, not unlike the exhumation of the lower units in a core complex environment (Kurz and Froitzheim, 2010). However, the study of Kurz et al. (2002) was done prior to the understanding of the 3D geometry of the shear zone published by Putz et al. (2006). Using this 3D model, it may be seen that the northernmost samples of Kurz et al. (2002) were sampled near the hanging wall of the shear zone and the southernmost samples near the foot wall (yellow stars on Fig. 2c). Potentially, this indicates a reversal of shear sense within the shear zone as it occurs during channel flow or other mechanisms that have previously been described in the literature (e.g., Passchier and Platt, 2017). Indeed, the model of Putz et al. (2006) shows that eclogite bodies occur both above the hanging wall and below the foot wall of the shear zone, which indicates that there is no appreciable difference in metamorphic grade between the sides of the shear zone (Fig. 2c).

The idea that shear sense reverses within the shear zone was tested by Eberlei et al. (2014) using barometric constraints on samples from the hanging wall and the foot wall of the Plattengneis shear zone. They showed that there is a measurable difference between (i) structural and (ii) barometric separation of the foot- and hanging-wall of the shear zone, implying substantial volume loss inside the shear zone, as may occur during channel flow (Fig. 2c, inset).

In the most recent development to date, Schorn and Stüwe (2016) investigated the field gradient across the Plankogel detachment, which is interpreted to be the downward continuation of the Plattengneis shear zone in the southern region of the Koralpe (Fig. 2c). Based on petrological observations they recognized a substantial loss of section across the Plankogel detachment and interpreted the Plattengneis shear zone and the Plankogel detachment to be the relict of an extraction fault in the sense of Froitzheim et al. (2003). Within this model the Plattengneis shear zone now receives a significant tectonic position as a major horizon during the early, south

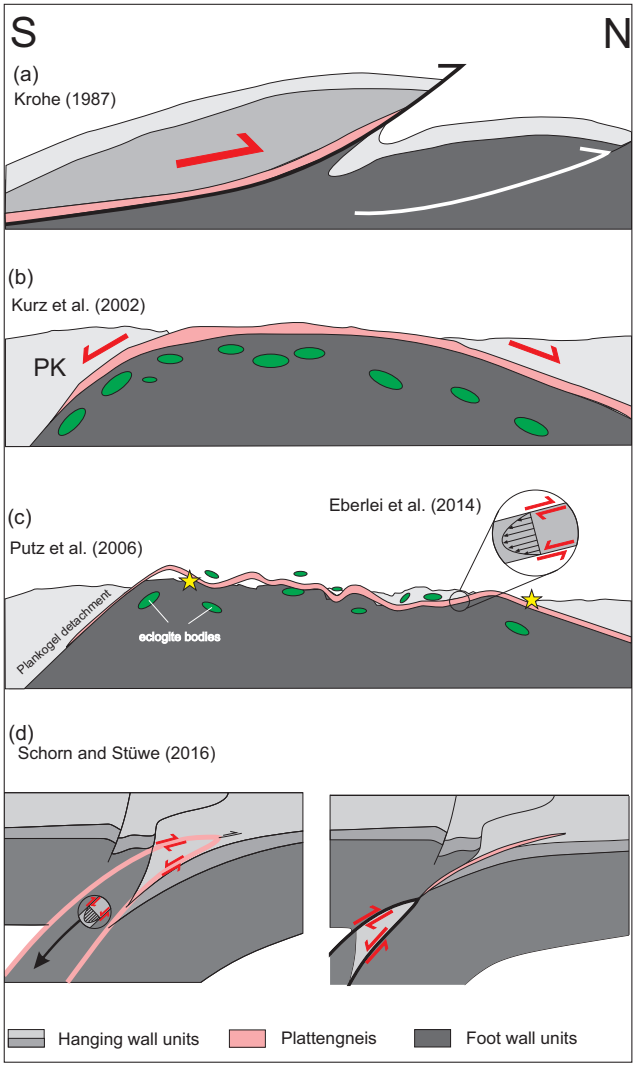

Figure 2: Development of models for the tectonic significance of the Plattengneis shear zone. **(a)** Krohe (1987) proposed a largely top-to-the-north shear sense and interpreted the shear zone as a major horizon during north directed nappe stacking. **(b)** Kurz et al. (2002) recognized a reversal of shear sense from south to north and inferred the shear zone to be responsible for the exhumation of the eclogite-facies rocks below (PK is the Plankogel complex). **(c)** Putz et al. (2006) first documented the 3D geometry of the shear zone and showed that eclogites (green ellipses) occur both above and below the shear zone. Note that the northernmost exposure of Plattengneis is its hanging wall and the southernmost is its foot wall (yellow stars). Eberlei et al. (2014) suggested that the observations of Kurz et al. (2002) were a reversal of shear sense within the shear zone (inset on (c)). **(d)** The model proposed by Schorn and Stüwe (2016) invokes slab extraction during the Eoalpine subduction and satisfies all earlier observations.

directed Eoalpine subduction from which a wedge-shaped crustal section was extracted downwards (Stüwe and Schuster, 2010; Schorn and Stüwe, 2016) (Fig. 2d). The model is not only consistent with the proposed shear sense reversal within the shear zone (Eberlei et al., 2014), but also with the general metamorphic field gradient (Tenczer and Stüwe, 2003; Herg and Stüwe, 2018). However, further evaluation of the shear sense changes with respect to the shear zone boundaries remains untested.

Because each of the above kinematic models (Fig. 2) has distinctive predictions for the distributions of deformational fabrics inside the shear zone, their validity can be assessed through determination of dominant shear sense. A quantitative evaluation of strain geometry must be done for carefully located samples, spread both vertically and horizontally throughout the Plattengneis shear zone. This study provides such an assessment by integrating LPOs of quartz, measured using EBSD, to characterize the 3D variability of deformational fabrics within the Plattengneis.

2. Approach and methods

For this study, 66 GPS-located, oriented samples throughout the Plattengneis shear zone were collected in the field (Fig. 3). Sample locations were systematically chosen using inferences from existing maps and the published work of Putz et al. (2006) to provide regional and vertical coverage of the shear zone. The samples were collected from four geographic regions of the shear zone, each of which was chosen so that a vertical transect across the shear zone could be sampled. The four geographical regions are the Schwanberg Synform transect (south); the Lassnitz Klause transect (east-central); the Pack Dome transect (north), and the Weinebene transect (west-central) (Fig. 3). Additional structural data collected in the field included 93 lineation measurements and 114 foliation measurements that were used for the 3D geometry modelling of the shear zone.

2.1. 3D Model input and parameters

To establish the three-dimensional distribution of deformational fabrics throughout the Plattengneis, it is necessary to know the position of each sample within the shear zone, which in turn requires knowledge of the zone's 3D geometry. The 3D geometry of the Plattengneis was first investigated by Putz et al. (2006), who combined mapped locations of contacts and detailed measurements of structural attitudes with a DEM using the commercial software package 3DGeoModeller (http://3dweg.brgm.fr/). Their model shows the Plattengneis to be a sub-horizontal zone, varying in thickness from 250 m to 600 m, that has been deformed by km-scale open folds along NW-SE axes that have only a few hundred meters amplitude (Fig. 4b). However, the Putz et al. (2006) model used a DEM with a resampled resolution of more than 100 m. Here we use an updated model of the shear zone with a 3'' arc second resolution surrounding the shear zone contacts and boundaries. Our model incorporates the input data used in Putz et al. (2006) with additional field measurements acquired for this study (Figs. 3, 4). The DEM comprised two merged Shuttle Radar Topography Mission (SRTM3) tiles, downloaded from ftp://ftp.glcf.umiacs.umd.edu/glcf/SRTM, that were projected to Universal Transverse Mercator (UTM) Zone 33 North, WGS84 coordinates (Gorokhovich and Vous-

tianiouk, 2006). All data were then entered into ArcGIS in order to: (i) organize and visualize the map layers; (ii) plot structural data of the Plattengneis on the maps; (iii) properly digitize contacts and (iv) prepare a DEM for import into the 3DGeoModeller software.

The variability of exposure of the shear zone in outcrop means that the form and structure may not always be visible in the field. Many 3D software programs are explicit, requiring this knowledge as input data for the model. 3DGeoModeller was chosen because it is an implicit geostatistical modeling software package that interpolates the geometry of the shear zone without having to define the form and structure of all surfaces being modeled. The 3DGeoModelling software instead uses three-dimen-

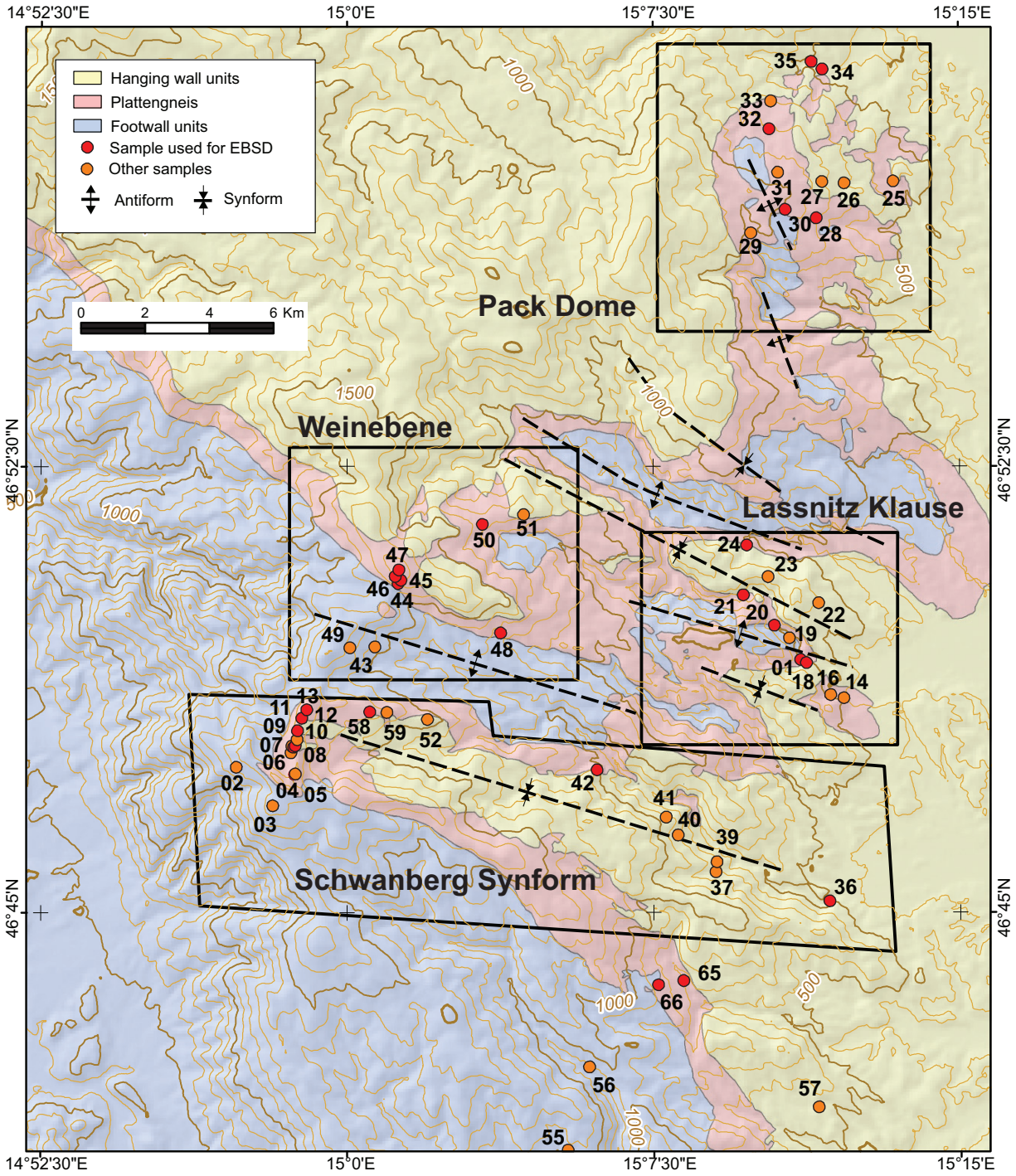

Figure 3: Map of the eastern Koralpe showing the sample locations and modelled Plattengneis distribution. Boxes locate the four geographically key regions chosen for this study: the Schwanberg Synform transect in the south, the Lassnitz Klause transect in the east-central, the Pack Dome transect in the north, and the Weinebene transect in the west-central.

sional input data to calculate a volume function that is then used to interpolate the full geometry of the shear zone (e.g., Lajaunie et al., 1997).

2.2. EBSD analysis of LPOs

For fabric analysis of the Plattengneis thin sections were cut perpendicular to foliation and parallel to lineation to facilitate optical examination of microstructures and EBSD analysis. Fabric analyses were conducted at the University of Texas at Austin using a Philips XL30 environmental scanning electron microscope (ESEM), in conjunction with an HKL Nordlys EBSD camera and HKL Channel 5 software package. Each sample was analyzed using the same set of ESEM parameters: accelerating voltage of 20 kV, a spot size setting of 6 and a pressure of 0.3 torr and variable working distance. The 'Tango' program within the HKL Channel 5 software was used to map quartz orientations in selected areas, and to reduce the full data set to a subset consisting of only one point per grain, defined as a minimum misorientation of 3°. The PFch5 software package (Mainprice, 2005) was used to construct logarithmic pole figures for further interpretation.

Much of the information contained in pole figures obtained from EBSD analysis is derived from an understanding of how the activation of different slip systems in quartz produces distinctive regions of increased density around the [*c*]-axis poles. Following Passchier and Trouw (2005) for non-coaxial deformation: *basal <a> slip* produces density of poles at the periphery of the pole figure near the Z-axis of the finite-strain ellipsoid; *rhomb <a> slip* produces density in the interior of the pole figure within the Y-Z plane of the finite-strain ellipsoid; *prism <a> slip* produces density near the center of the pole figure, close to the Y-axis of the finite-strain ellipsoid; and *prism [c] slip* produces density at the periphery of the pole figure near the X-axis of the finite-strain ellipsoid. In this paper, logarithmic plots that display the <001> or [*c*]-axis distribution, and the <100> or <*a*>-axis distributions will be described in terms of the activated slip systems inferred from pole figure density diagrams.

Beyond the interpretation of shear sense, the activation of different slip systems during deformation can be used as an indicator of deformation temperature and additional controls like strain rate, differential stress or water content may also influence slip system activation. In the discussion section of this paper deformation temperature estimates will be based on the regimes defined by Hirth and Tullis (1992), and the relation of recovery and recrystallization temperatures from Stipp et al. (2002) and Passchier and Trouw (2005).

2.3. Strain geometries from Vollmer diagrams

Further information on the strain geometry of a fabric is interpreted using Vollmer diagrams (Vollmer, 1990). For this diagram, the PFch5 program calculates three values that describe the fraction of the pole figure density distribution that can be accounted for by a point maximum (indicating a single orientation of most grains as in plane strain *P*), by a girdle (generally indicating flattening or constriction *G*), and by a random distribution (*R*). The portion of the density distribution that is non-random is a measure of the strength of the LPO and can be expressed as the quantity (1-*R*). Vollmer's (1990) triangular diagram with apices *P*, *G*, and *R* uses the relative values of these quantities to infer the geometry of the strain implied by the distribution of densities within the pole figures. Our use of these diagrams follows the interpretation of strain geometry from Barth et al. (2010). Differences in strain geometries correspond to differences in two normalized values, *Pn* and *Gn*, which disregard the random component of the pole figure. These two parameters are defined as $Pn = P/(P+G)$ and: $Gn = G/(P+G)$. The strength of the LPO will also be measured in terms of "multiples of uniform density" (m.u.d. values).

For fabrics showing specific slip systems, the *Pn* and *Gn* values help to evaluate whether the fabric is indicative of plane strain, or of constriction/flattening. For a dominant prism <*a*> slip system, a high *Pn* value indicates plane strain and a low *Pn* value indicates flattening or constriction, which can be further interpreted based on the orientation of the [*c*]-axis girdle with respect to foliation. Fabrics in which the majority of the *c*-axis poles lie in the Y-Z plane of the finite-strain ellipsoid exhibit a component of constriction; fabrics in which the majority of the *c*-axis poles lie in the X-Y plane of the finite-strain ellipsoid exhibit a component of flattening (Barth et al., 2010).

3. Petrography and sample selection

The Plattengneis is commonly distinguishable in outcrop from surrounding units by its distinct mylonitic fabric and strong lineation defined by elongated feldspars trending in a north-south orientation. The shear zone samples record upper amphibolite- to eclogite-facies metamorphism (Tenczer and Stüwe, 2003). The common mineral assemblage for the Plattengneis is quartz + garnet + muscovite + plagioclase + biotite + ilmenite ± kyanite ± chlorite ± rutile. In thin section, all samples show a well-developed foliation defined by layers of recrystallized quartz and feldspar alternating with layers of aligned biotite, muscovite and kyanite; garnet and plagioclase are present as porphyroclasts. Both in outcrop and thin section the Plattengneis lacks unambiguous shear sense indicators. More details on petrography of the rocks and their microstructures were discussed at length by Krohe (1987), Hoinkes et al. (1999), Kurz et al. (2002) and references therein.

All thin sections used in the interpretation here contain quartz and feldspar grains that show evidence for recovery and dynamic recrystallization. Within the matrix, the fine-grained quartz and feldspar grains have uniform sizes and shapes with both straight and irregular grain boundaries. Less commonly, these fine grains exhibit recovery as shown by discontinuous undulatory

extinction and subgrains. The quartz grains range in size from ~400 µm in the dynamically recrystallized layers of the fine-grained matrix to ~4 mm in the coarse-grained layers (Fig. 5a). In the coarse-grained, quartz-rich layers, quartz may form elongate or ribbon-shaped grains that commonly exhibit discontinuous undulatory extinction and subgrains. The coarse-grained quartz crystals exhibit interfingering, interlobate to amoeboid shapes with variable sizes, and typically lack core-mantle structures (Fig. 5b). The medium-sized, elongate feldspars commonly show discontinuous undulatory extinction, minor subgrains and incipient core-mantle structures. The feldspar porphyroclasts exhibit recrystallization by bulging boundaries, in addition to recovery features such as undulose extinction, subgrains and core-mantle structures (Fig. 5c).

Selection of samples for this paper was based on the following criteria: (i) Presence of a distinct foliation and prominent N-S trending lineation in outcrop. (ii) Presence of a distinct mylonitic fabric in thin section and the characteristic mineral assemblage listed above. (iii) Visibility of a preferred orientation present in the quartz grains in thin section with the insertion of a gypsum plate. (iv) An EBSD analysis derived pole figure with a well-defined fabric. (v) A sample location within or near the modelled Plattengneis shear zone. All 66 samples collected were examined for these criteria and 40 samples were removed having not met all criteria. The remaining 26 were used in the final interpretation as the best representatives of the Plattengneis and are presented below.

4. Results

The results of this study are two-fold. Firstly, the modeled 3D distribution of the Plattengneis will be presented. Secondly, quartz LPOs of the selected 26 samples will be presented in the form of pole figures arrayed according to their vertical locations within the shear zone and by their respective transects.

4.1. 3D Geomodel of the Plattengneis

The shear zone geometry was constructed within a model volume 30 km by 30 km in area and 10 km in thickness and is presented in Figure 4. The boundaries of the modeled area fall within 50 m of those from Putz et al. (2006). Differences from Putz et al. (2006) of the modeled surface distribution of the Plattengneis can be attributed to the somewhat higher resolution DEM used here. The final 3D model (Figs. 3, 4) shows the contacts in relation to the topography and depth, allowing construction of cross sections in any orientation through the model volume. These cross sections were used to determine the vertical location of each sample as well as the thickness of the shear zone at the sample location (Fig. 6). Overall, the model shows that the shear zone is consistently between 300 m and 500 m thick over the entire region and that it is largely made up of a single shear horizon.

The model of the 3D geometry of the Plattengneis produced in this study agrees very well with the distribution of the shear zone as previously mapped in the field (Flügel and Neubauer, 1984; red lines on Fig. 4). Differences in the surface exposure of the shear zone are a result of the shear zone being nearly horizontal, so that intersections of the contact between the upper unit and the Plattengneis with topography vary strongly with the model resolution (Putz et al., 2006). Moreover, minor secondary strands of the shear zone occur in several places as schematically indicated in pink on Figure 4b.

4.2. Fabric data by transect

Pole figures for the 26 selected samples are presented in Figure 7. All of the pole figures are logarithmic plots that display the <001> or [*c*]-axis distribution (pole figure on left), and the <100> or <*a*>-axis distribution (pole figure on right). Figures 5 and 6 show that ten samples were selected from the Schwanberg Synform region, five from the Lassnitz Klause region, five from the Pack Dome region and six from the Weinebene region. Overall, these samples reflect a good representation of different vertical positions within the shear zone (Fig. 6). Additionally, most fabrics display dominant prism <*a*> slip and are therefore plotted on prism <*a*> Vollmer diagrams (Fig. 8). The fabrics are characterized as being either symmetric or asymmetric. Asymmetric fabrics are those in which the *c*-axis maximum falls at an acute angle to the Y-Z plane of the finite-strain ellipsoid, and the strongest *a*-axis maximum is at an acute angle to the Y-X plane of the finite-strain ellipsoid.

Within the ***Schwanberg Synform transect***, the modeled thickness of the shear zone ranges from 289 m to 468 m. The ten samples that make up this transect, listed from top to bottom of the shear zone, are: KA08-66, KA08-07, KA08-08, KA08-65-02, KA08-12, KA08-58, KA08-11, KA08-10, KA08-42 and KA08-36 (Figs. 6–8). All of the quartz fabrics within this transect have a strong LPO: maximum values of the m.u.d. in the *c*-axis pole figures range from 4.45 to 9.75; those for *a*-axis pole figures range from 2.56 to 7.77. The *c*-axis pole figures in this transect show dominant prism <*a*> slip in addition to faint basal <*a*> slip or rhomb <*a*> slip. For five of the ten *a*-axis pole figures (KA08-66, KA08-65-02, KA08-12, KA08-42 and KA08-36), some density appears within the interior of the pole figure, as opposed to only being on the periphery. All of the *a*-axis pole figures display three peripheral maxima with a strong *a*-axis maximum that is asymmetric to the foliation plane.

Within the ***Lassnitz Klause transect***, the modeled thickness of the shear zone ranges from 326 m to 396 m. The five samples that make up this transect, listed from top to bottom of the shear zone, are: KA08-20, KA08-24, KA08-01, KA08-21 and KA08-18 (Figs. 6–8). All of the quartz fabrics within this transect have a strong LPO: maximum values of the m.u.d. in the *c*-axis pole figures range from 4.33 to 7.56; those for *a*-axis pole figures

range from 2.26 to 3.34. The *c*-axis fabrics for the pole figures in this transect show dominant prism <*a*> slip with basal <*a*> slip as a secondary maximum, and three of the pole figures also display faint to moderate rhomb <*a*> slip. All of the *a*-axis pole figures have some density in the interior of the pole figure, with three maxima on, or close to, the periphery of the pole figure and only three of the five samples showing a strong *a*-axis maximum (KA08-01, KA08-21, and KA08-18). All five samples in this transect are asymmetric to the foliation plane.

Within the ***Pack Dome transect***, the modeled thickness of the shear zone ranges from 281 m to 292 m. The five samples that make up this transect, listed from top to bottom of the shear zone, are: KA08-30, KA08-28, KA08-

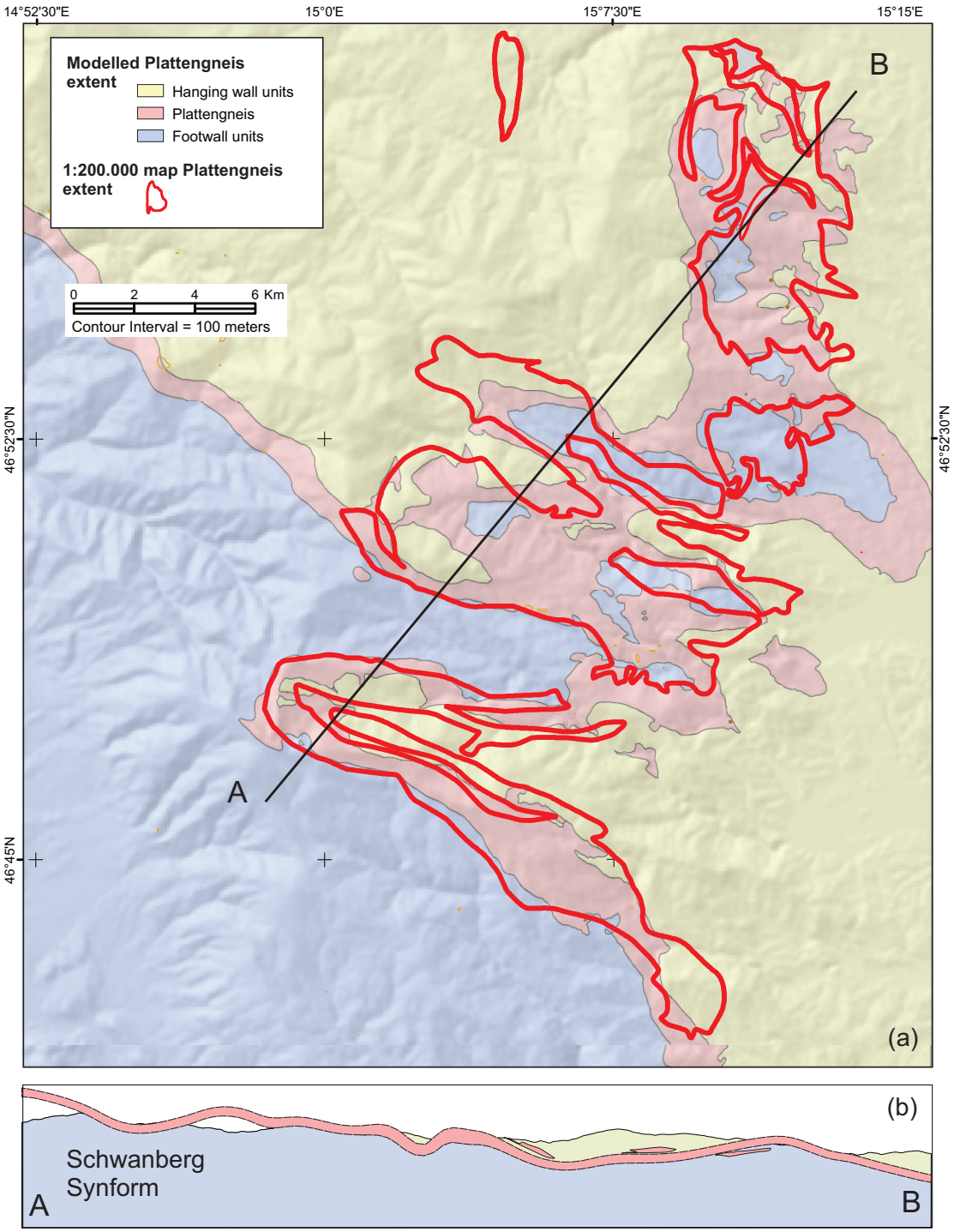

Figure 4: Comparison between modelled (map colors) and mapped (thick red lines) distribution of Plattengneis. **(a)** 2D map. The red lines are the georeferenced outlines of the Plattengneis distribution of the Geological Map of Steiermark (Flügel and Neubauer, 1984). **(b)** Cross section along line A-B. Modelled Plattengneiss on (b) is the red zone.

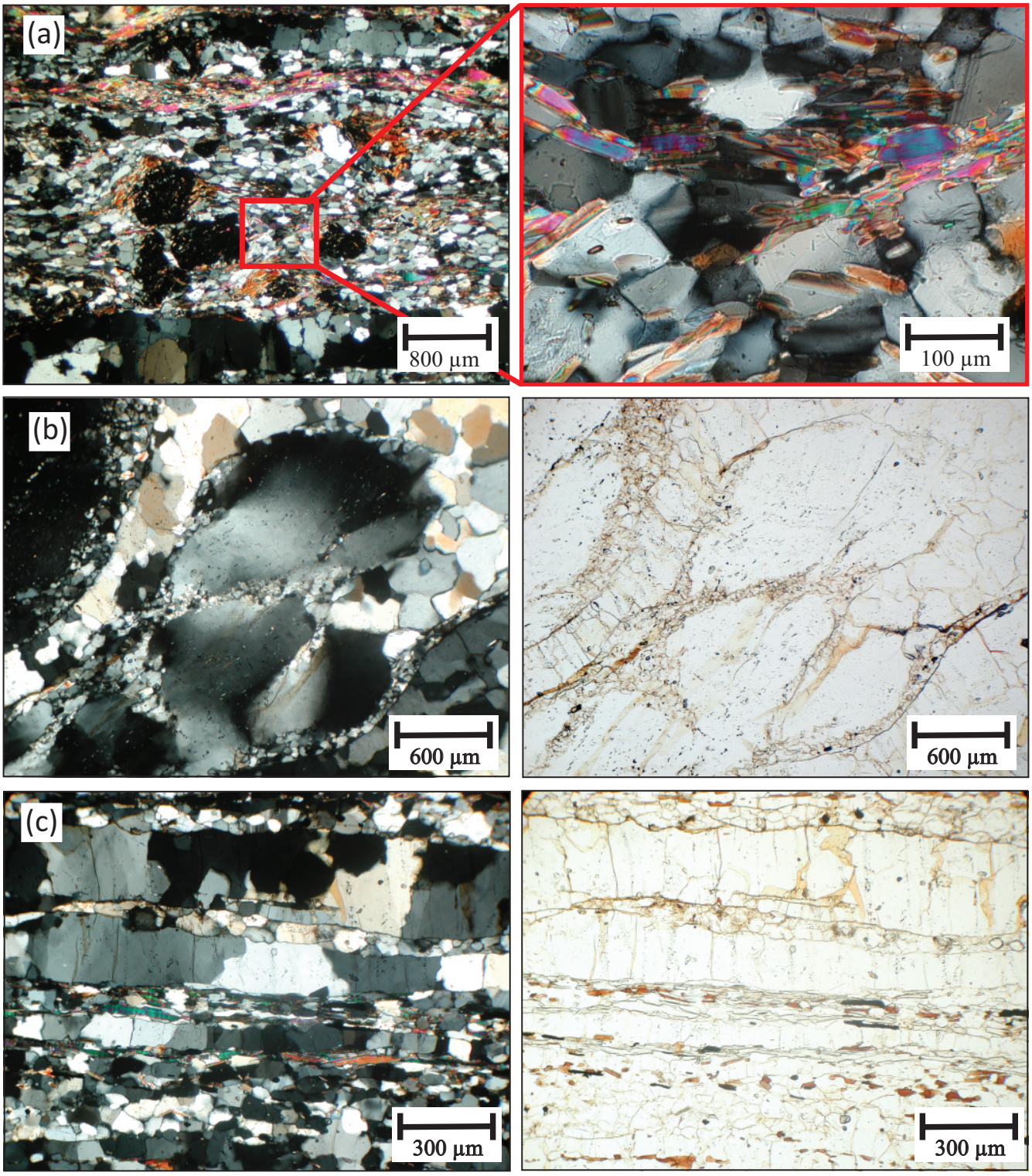

Figure 5: Photomicrographs of fabrics in the Plattengneis. **(a)** Thin section photomicrographs of sample KA08-07 in circular polarized light. On the left is an image capturing the characteristic fabric of the Plattengneis containing a fine-grained quartz and plagioclase matrix and foliation made up of quartz veins alternating with layers of aligned micas and garnet porphyroblasts. The enlargement of the red box on the right shows the undulose extinction and subgrains within the fine-grained quartz and feldspar grains. **(b)** Characteristic dynamic recrystallization of feldspars in the Plattengneis with feldspar porphyroclasts displaying bulging boundaries, undulose extinction, subgrains and core-mantle structures. Circular polarized light on left and plane polarized light on right. **(c)** Image of quartz grains showing typical interfingering, interlobate to amoeboid shapes and variable sizes defining recrystallization. Circular polarized light on left and plane polarized light on right.

32, KA08-34 and KA08-35 (Figs. 6–8). All of the quartz fabrics within this transect have a strong LPO: maximum values of the m.u.d. in the *c*-axis pole figures range from 4.62 to 6.94; those for *a*-axis pole figures range from 2.78 to 3.95. The *c*-axis fabrics for the pole figures in this transect have dominant prism <*a*> slip in addition to rhomb <*a*> slip, or a combination of basal <*a*>, rhomb <*a*>, and prism <*a*> slip. All of the *a*-axis pole figures display some density in the interior of the pole figures, and none of them have three well-defined maxima around the periphery. All five pole figures show a strong *a*-axis maximum that is asymmetric to the foliation plane.

Within the ***Weinebene transect***, the modeled thickness of the shear zone ranges from 294 m to 500 m. The six samples that make up this transect, listed from top to bottom of the shear zone, are: KA08-48, KA08-44, KA08-46, KA08-45, KA08-50 and KA08-47 (Figs. 6–8). All of the quartz fabrics within this transect have a strong LPO: maximum values of the m.u.d. in the *c*-axis pole figures range from 4.94 to 10.57; those for *a*-axis pole figures range from 2.94 to 5.78. The *c*-axis fabrics for the pole figures in this transect have dominant prism <*a*> slip in addition to basal <*a*> or rhomb <*a*> slip, or a combination of basal <*a*>, rhomb <*a*> and prism <*a*> slip. Four of the six *a*-axis pole figures display low densities in the interior of the pole figures (KA08-44, KA08-45, KA08-50 and KA08-47), and all six have three well-defined maxima surrounding the periphery. Four of the pole figures show a strong *a*-axis maximum that is slightly asymmetric to the foliation plane (KA08-44, KA08-46, KA08-45 and KA08-47), and two pole figures are symmetric (KA08-48 and KA08-50).

Although there are differences from sample to sample in the fabrics seen in the pole figures of quartz LPOs (Fig. 7), some observations are common to all of them. On *c*-axis pole figures, the greatest density of poles is commonly near the center of the diagram, with lower densities occasionally found along the Y-Z plane in the interior of the diagram and/or at the periphery of the diagram near the Z-axis. Thus, the dominant slip system in almost all cases is prism <*a*>, together with subsidiary basal <*a*> slip, rhomb <*a*> slip, or a combination of all three. The *a*-axes commonly exhibit a strong maximum that is asymmetric to the foliation plane. Some *a*-axis pole figures have, in addition, low but appreciable densities in their interiors. All of the quartz fabrics within the Plattengneis have a strong LPO: maximum values of the m.u.d. in the *c*-axis pole figures range from 4.33 to 10.57; those for *a*-axis pole figures range from 2.26 to 7.77. All LPO strengths, calculated as (1-*R*), are greater than 0.5, with the exception of five samples whose values fall between 0.36 and 0.5 (Figs. 7, 8).

5. Discussion

Because different slip systems are activated at different temperatures, estimates of temperature accompanying deformation can be extracted from the distributions of densities in the pole figures. Using previously published data we suggest that a conceptual synthesis of prior eval-

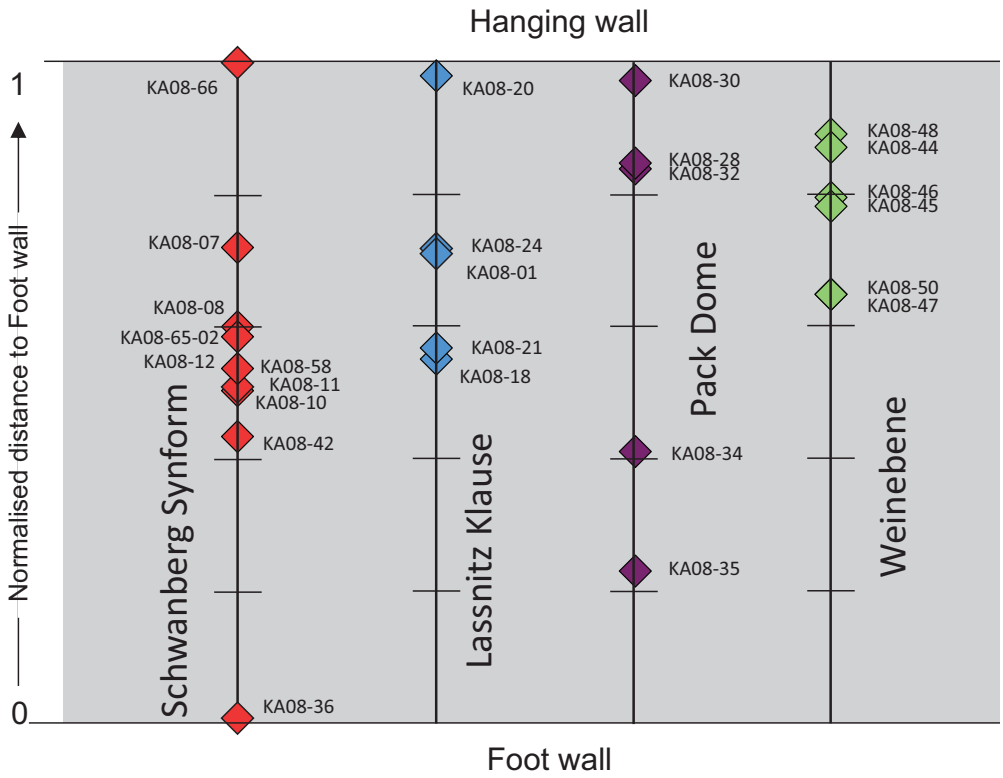

Figure 6: Position of the 26 samples used for fabric analysis in this study relative to the modelled shear zone boundaries.

uations – one accounting specifically for the character of transitional features – is helpful to properly interpret the fabrics for non-coaxial shear present in the Plattengneis. For this, we find it useful to base our interpretation on the conceptual synthesis shown in Figure 9, which focuses on the character of multiple transitional fabrics that may be intermediate in terms of mechanisms of dynamic recrystallization and the dominantly activated slip systems. We have chosen to categorize fabrics using the six following types (Fig. 9):

Type A is an end-member fabric that corresponds to the lowest temperatures of deformation, below 400 °C, in which recrystallization by bulge nucleation (BUL) is prevalent. In the *c*-axis figures, fabrics display a maximum on the periphery of the pole figure in addition to a maximum parallel to the Y-axis of the finite-strain ellipsoid, indicative of basal <*a*> and prism <*a*> slip; three *a*-axis maxima appear at the periphery with low densities in the interior (Barth et al., 2010).

Type B are transitional fabrics that represent the change from low to medium temperatures, between ~400 °C and 500 °C. They are characterized by the dominance of asymmetric crossed girdles or single girdles in which multiple slips may be activated, most commonly the combination of rhomb <*a*> and prism <*a*> slips (Stipp et al., 2002; Passchier and Trouw, 2005). These fabrics correspond to the temperatures of deformation at which subgrain rotation (SGR) is active.

Type C begins at the onset of medium-temperature deformation, occurring around 500 °C. It is clearly defined in the literature as a *c*-axis fabric with a single maximum parallel to the Y-axis of the finite-strain ellipsoid, indicating dominant prism <*a*> slip, with three *a*-axis maxima at the periphery of the pole figure (Stipp et al., 2002; Passchier and Trouw, 2005; Barth et al., 2010). Stipp et al. (2002) interpret prism <*a*> slip to take place at the same deformation temperatures as grain boundary migration (GBM) rather than SGR, however, at medium temperatures both SGR and GBM occur, as seen in regime 3 of Hirth and Tullis (1992).

Type D fabric shows the transition from medium to high temperatures (Fig. 9). In this temperature range, another transitional fabric, namely "mixed <*a*> slip", appears in accordance with the dominance of GBM and the faint operation of SGR (Barth et al., 2010). The "mixed <*a*> slip" fabric may be interpreted as the transitional fabric after prism <*a*> slip, marking the change from GBM I (~500 °C to ~630 °C) to GBM II (~630 °C to ~700 °C) (Stipp et al., 2002). The *c*-axis fabric shows the activation of basal <*a*>, rhomb <*a*>, and prism <*a*> slips as maxima in the Y-Z plane of the finite-strain ellipsoid, and three *a*-axis maxima occur at the periphery with low densities in the interior of the pole figure.

Type E is another transitional fabric indicating the onset of high temperatures (Stipp et al., 2002; Passchier and Trouw, 2005), related to GBM II by Stipp et al. (2002). In the *c*-axis pole figure there is a dominant maximum parallel to the Y-axis of the finite-strain ellipsoid, indicating prism <*a*> slip, together with one or two secondary maxima on the periphery of the pole figure, indicative of basal <*a*> and prism [*c*] slip. This fabric develops at temperatures approaching ~700 °C, the same temperatures at which GBM is the dominant active recrystallization process. It may also be interpreted as a transitional fabric from "mixed <*a*> slip" to dominant prism [*c*] slip.

Type F is seen at the highest temperatures, above ~700 °C. It is agreed in the literature that the *c*-axis pole figure exhibits a single maximum at the periphery, indicative of prism [*c*] slip, with three maxima in the *a*-axis near the Y-Z plane of the finite-strain ellipsoid (Stipp et al., 2002; Passchier and Trouw, 2005; Barth et al., 2010).

5.1. Plattengneis fabrics: temperatures of deformation, strain geometry and shear sense

Due to the presence of dominant prism <*a*> slip in almost all pole figures, a subdivision of the pole figures may be based on the slip systems that are activated in addition to prism <*a*> slip. The strain geometry is determined using the *Pn* and *Gn* values, as well as where the samples plot on a prism <*a*> Vollmer diagram (Fig. 8). Table 1 summarizes key observations and interpretations from the fabric analysis of the 26 samples of Plattengneis that form the core of this work. Using the framework summarized in Figure 9, data for each of the four sample transects is interpreted below. Note, however, that there appears no strong correlation between fabric type and either strain geometry or LPO strength as defined by the *Gn* or (1-*R*) parameters as explained above for any of the four transects (Fig. 10).

For the ***Schwanberg Synform transect***, the *c*-axis pole figures show dominant prism <*a*> slip in addition to faint basal <*a*> slip or rhomb <*a*> slip, but can be further divided into fabrics recognized as Type B, Type C and Type D. Samples KA08-07, KA08-08, KA08-10, KA08-11 and KA08-58 yield Type B fabrics; samples KA08-36, KA08-42 and KA08-65-02 yield Type C fabrics; and samples KA08-12 and KA08-66 yield Type D fabrics (Fig. 8). This suite of fabrics is interpreted to represent deformation at temperatures that range from slightly above 500 °C to ~630 °C. This is consistent with petrological estimates for the peak of metamorphism indicating that deformation occurred near peak metamorphism. The quartz LPOs are consistent with strain geometries that are dominated by non-coaxial deformation but involve appreciable constriction (Figs. 8, 10). This matches the interpretation of Eberli et al. (2014). Asymmetry is evident in the pole figures for all ten samples, of which seven imply a top-to-the-north shear sense, and three imply a top-to-the-south shear sense (Fig. 7).

For the ***Lassnitz Klause transect***, *c*-axis fabrics for the pole figures show dominant prism <*a*> slip with basal <*a*> slip as a secondary maximum, and three of the pole figures also display faint to moderate rhomb <*a*> slip. Although all samples display dominant prism <*a*> slip, this suite of fabrics can be further divided into fabrics recognized as Type D or transitional from Type D to Type E

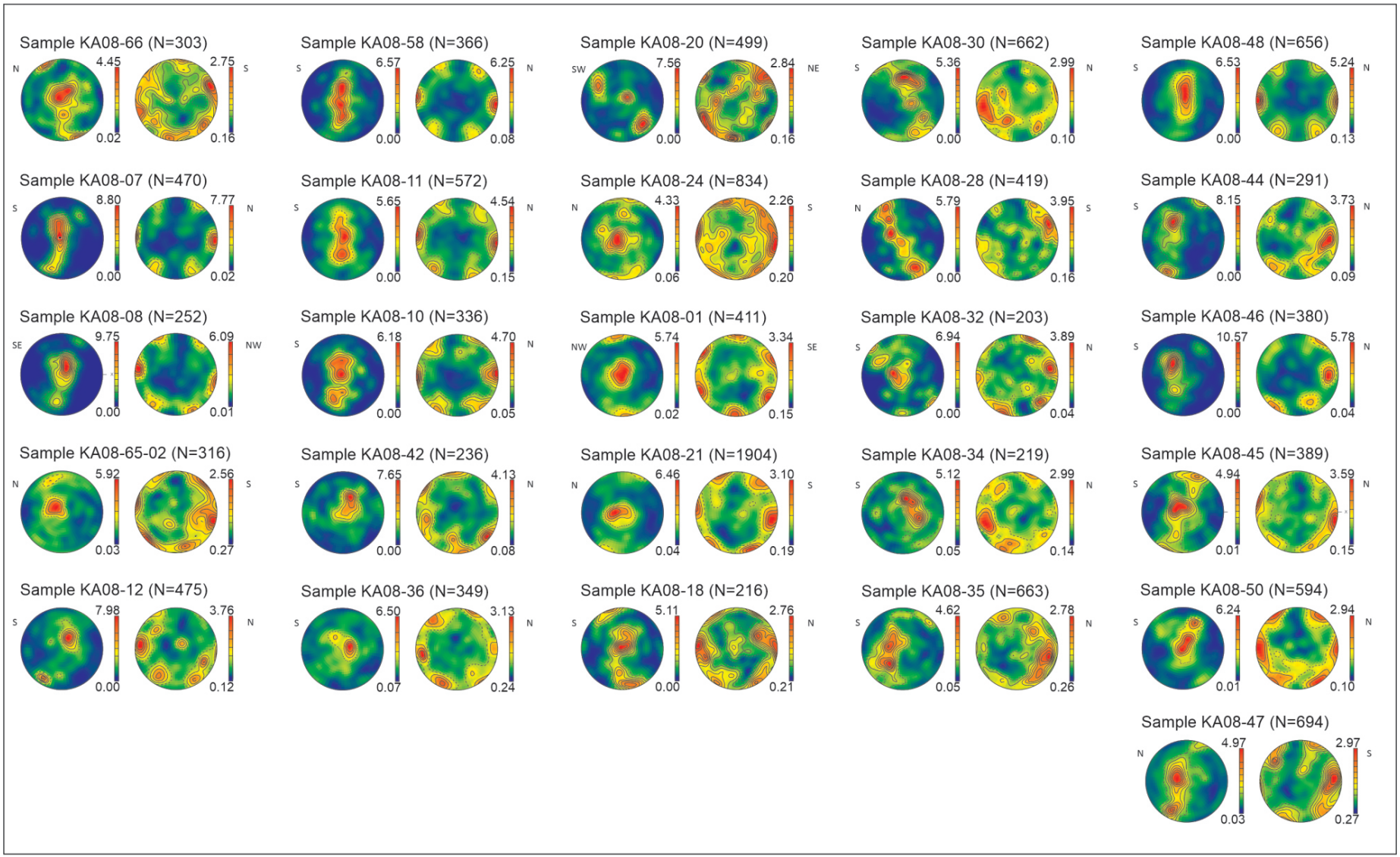

Figure 7: Results of EBSD measurements for the 26 samples collected from the four identified key regions. Pole figure results for each sample, shown with its *c*-axis (left) and *a*-axis (right).

(here, Type D-E). Samples KA08-18, KA08-20 and KA08-24 yield Type D fabrics; and samples KA08-01 and KA08-21 yield Type D-E fabrics (Fig. 8, Tab. 1). These two Type D-E fabrics superficially resemble Type A, but the foregoing analysis of recovery and recrystallization, particularly easy GBM, indicates temperatures higher than those associated with Type A fabrics. The transition from Type D to Type E fabrics consists of the loss of rhomb <*a*> slip and the addition of prism [*c*] slip. In these fabrics there is evidence for this transition as the rhomb <*a*> slip is no longer present and prism [*c*] slip is not yet evident. These are interpreted to be the highest-temperature fabrics,

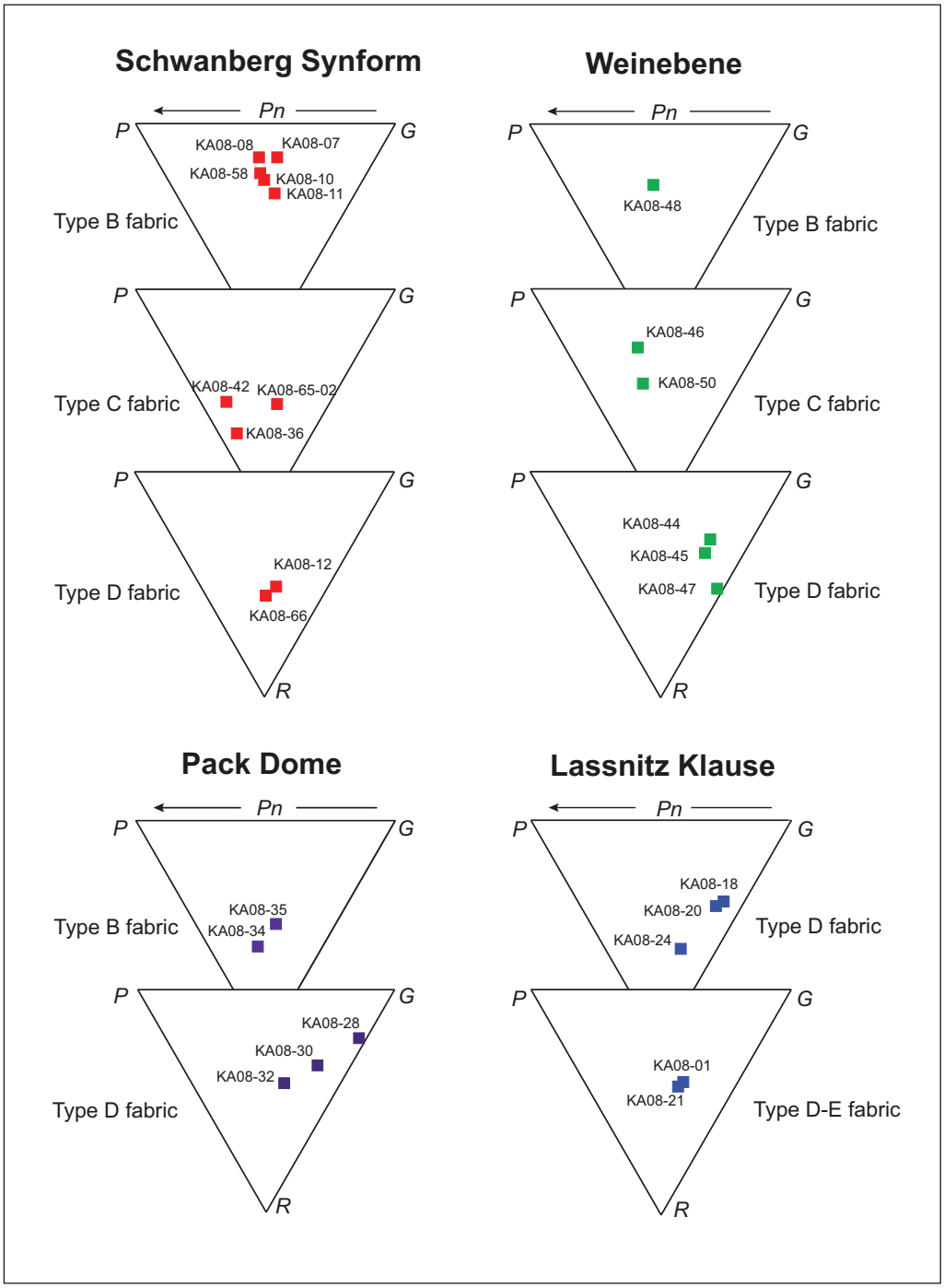

Figure 8: Vollmer diagrams. For the Schwanberg Synform transect, samples fall into three categories: Type B fabric – transition from low to medium temperatures. Type C fabric – medium temperatures. Type D fabrics – transition from medium to high temperatures. For the Lassnitz Klause transect, samples fall into two categories: Type D fabric – transition from medium to high temperatures. Type D-E fabric – transition from medium to high temperatures. For the Pack Dome transect, samples fall into two categories: Type B fabric – transition from low to medium temperatures. Type D fabric – transition from medium to high temperatures. For the Weinebene transect, samples fall into three categories: Type B fabric – transition from low to medium temperatures. Type C fabric – medium temperatures. Type D fabric – transition from medium to high temperatures.

Transect	Fabric Type	Sample Number	Shear Sense Top to:	Strength of LPO (1-*R*)	Constriction (*Gn*)*	Height Above Base of Shear Zone (m)
Schwanberg Synform (Fig. 7c)	B	KA08-07	north	0.85	0.55	172
		KA08-08	north	0.85	0.47	240
		KA08-10	south	0.75	0.49	289
		KA08-11	north	0.69	0.56	291
		KA08-58	north	0.78	0.47	322
	C	KA08-36	south	0.36	0.19	900
		KA08-42	north	0.50	0.19	476
		KA08-65-02	north	0.49	0.59	251
	D	KA08-12	north	0.62	0.70	266
		KA08-66	south	0.45	0.51	17
Lassnitz-Klause (Fig. 8c)	D	KA08-18	south	0.64	0.88	355
		KA08-20	south	0.62	0.84	32
		KA08-24	north	0.43	0.67	200
	E	KA08-01	north	0.59	0.64	224
		KA08-21	south	0.57	0.61	288
Pack Dome (Fig. 9c)	B	KA08-34	north	0.44	0.42	326
		KA08-35	north	0.54	0.58	436
	D	KA08-28	north	0.78	0.96	101
		KA08-30	north	0.66	0.80	31
		KA08-32	north	0.58	0.62	104
Weinebene (Fig. 10c)	B	KA08-48	-	0.72	0.46	77
	C	KA08-46	north	0.74	0.37	215
		KA08-50	-	0.58	0.39	274
	D	KA08-44	north	0.70	0.76	143
		KA08-45	north	0.64	0.77	233
		KA08-47	north	0.57	0.66	382

*Values above 0.5 indicate that constriction dominates over plane strain; larger values indicate greater constriction.

Table 1: Summary of key observations and interpretations of the samples collected and evaluated for further fabric analysis in this study.

representing temperatures that fall between ~630 °C to slightly below 700 °C. The quartz LPOs are consistent with strain geometries that are dominated by non-coaxial deformation but involve a component of constriction (Figs. 8, 10). Asymmetry is evident in the pole figures for all five samples. Three samples, KA08-20, KA08-21 and KA08-18, show asymmetry favoring a top-to-the-south shear sense and the remaining two samples exhibiting a top-to-the-north shear sense (Fig. 7).

For the ***Pack Dome transect*** the *c*-axis fabrics for the pole figures show dominant prism <*a*> slip in addition to rhomb <*a*> slip, or a combination of basal <*a*>, rhomb <*a*>, and prism <*a*> slip. These samples can be divided into fabrics recognized as Type B and Type D. Samples KA08-34 and KA08-35 yield Type B fabrics; and samples KA08-28, KA08-30 and KA08-32 yield Type D fabrics (Fig. 8). This suite of fabrics is interpreted to represent deformation at temperatures that range from slightly below 500 °C to around 630 °C. The quartz LPOs are consistent with strain geometries that are dominated by non-coaxial deformation but involve appreciable constriction (Figs. 8, 10). Asymmetry is evident in the pole figures, which

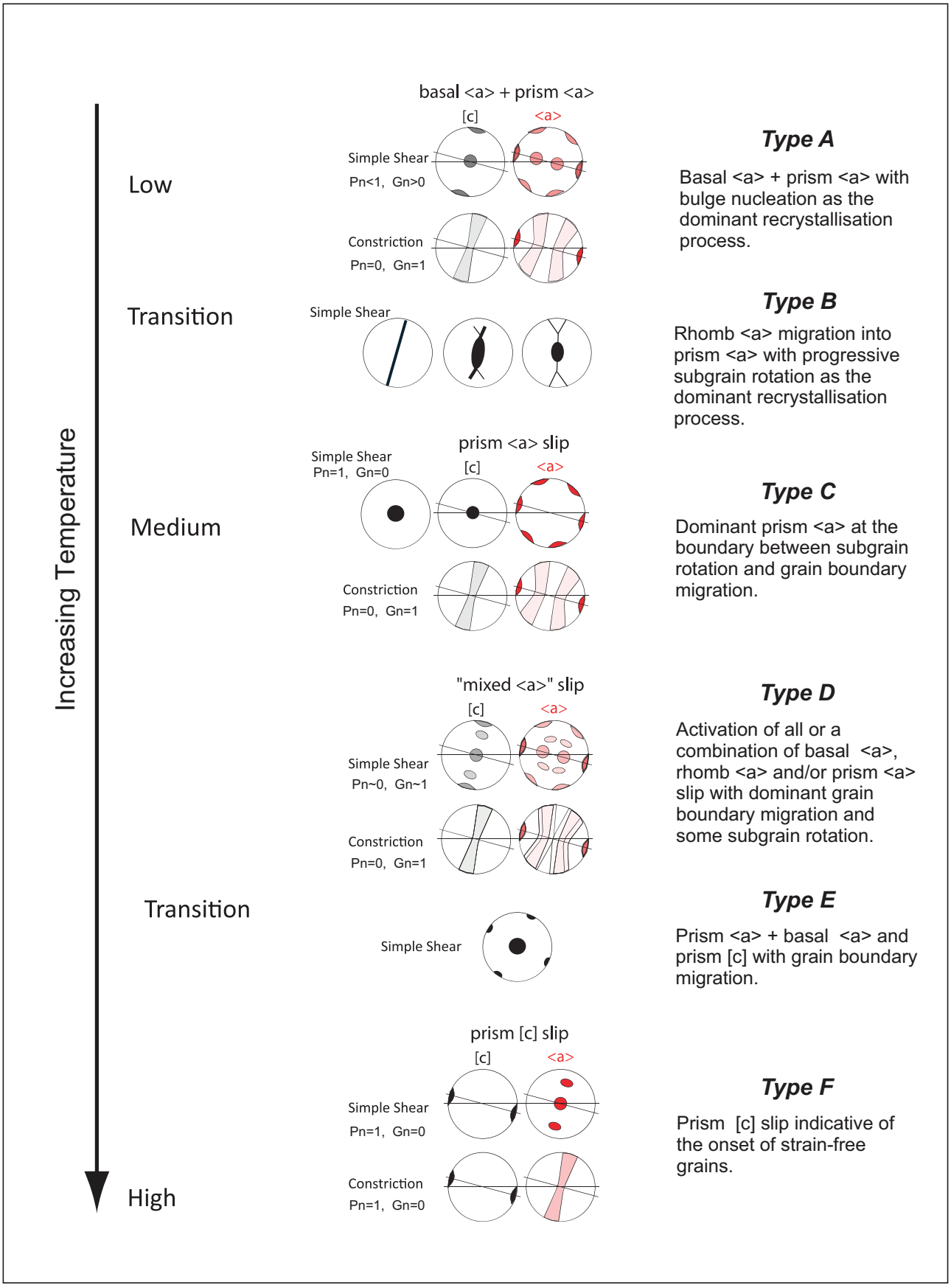

Figure 9: Synthesis of different quartz LPO fabrics including transitional fabrics. The figure is a combination of Figure 14b from Stipp et al., (2002) and Figure 1 from Barth et al., (2010), simple shear and non-coaxial + constriction. This chart shows the progression of fabrics, activated slip systems, temperatures and recrystallization processes with increasing temperatures.

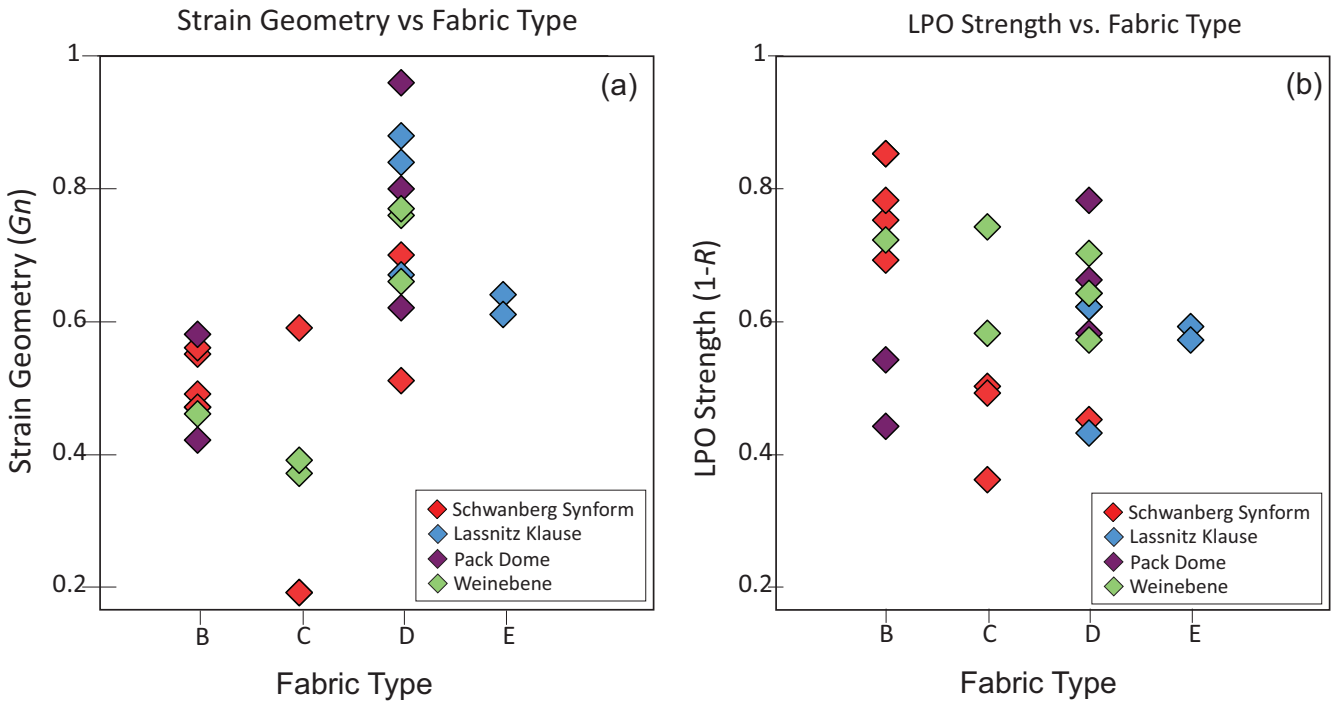

Figure 10: (a) Graph showing strain geometry (*Gn*) vs. temperature (fabric type). **(b)** Graph showing LPO strength (1-*R*) vs. temperature (fabric type).

for all five samples imply a top-to-the-north shear sense (Fig. 7).

For the ***Weinebene transect***, the *c*-axis fabrics for the pole figures show dominant prism <*a*> slip in addition to basal <*a*> or rhomb <*a*> slip, or a combination of basal <*a*>, rhomb <*a*> and prism <*a*> slip and can be characterized as Type B, Type C or Type D fabrics. Sample KA08-48 yields a Type B fabric; samples KA08-46 and KA08-50 yield Type C fabrics; and samples KA08-44, KA08-45 and KA08-47 yield Type D fabrics (Fig. 8). This suite of fabrics is interpreted to represent temperatures that range from slightly above 500 °C to around 630 °C. The quartz LPOs are consistent with strain geometries that are dominated by non-coaxial deformation but involve a component of constriction (Figs. 8, 10). Asymmetry is evident in the pole figures for four of the six samples, of which all four imply a top-to-the-north shear sense (Fig. 7).

5.2. Temperature, strain geometry and intensity of deformation

To investigate possible relationships among temperature, strain geometry, and intensity of deformation, correlations were sought (1) between temperature (fabric type: B, C, D, or E) and the strain geometry (*Gn*); and (2) between temperature (fabric type: B, C, D, or E) and LPO strength, both as a function of vertical position in the shear zone (Fig. 6). The array of data in Figure 10a suggests that the constrictional phase of Plattengneis deformation corresponds to the higher-temperature portion of the deformational history. Both the interpreted temperatures and the fact that a significant constriction is evident for most samples matches the interpretation of petrological peak metamorphic estimates and the tectonic interpretation of Eberli et al. (2024), respectively. However, no relationship is evident in Figure 10b between temperature and the intensity of deformation as indicated by LPO strength. The intensity of deformation as indicated by the strength of the quartz LPOs shows also little correlation with the vertical position of a sample within the shear zone (Fig. 11). Strain geometry, as reflected in values of *Gn* and *Pn*, similarly lacks correlation with vertical position.

5.3. Summary of findings

Both thin-section observations and quartz LPOs provide evidence that deformation of the Plattengneis occurred at medium to high temperatures, falling principally in the range of ~500 °C -700 °C. Key indicators for this temperature range are the dominant presence of GBM and some SGR recrystallization, in association with the majority of pole figure fabrics exhibiting *c*-axis patterns with dominant prism <*a*> slip, and the combination of basal <*a*>, rhomb <*a*> and prism <*a*> slips together with *a*-axis pole figures exhibiting a single dominant *a*-axis maximum at the pole figure periphery. The temperature interpretations based on these fabrics are also consistent with the north-south metamorphic temperature gradient found in Tenczer and Stüwe (2003). We interpret this as additional evidence that deformation of the Plattengneis occurred near the peak of metamorphism.

With respect to shear sense, both top-to-the-north and top-to-the-south shear senses are present, but top-to-the-north shear senses dominate: this sense of shear is

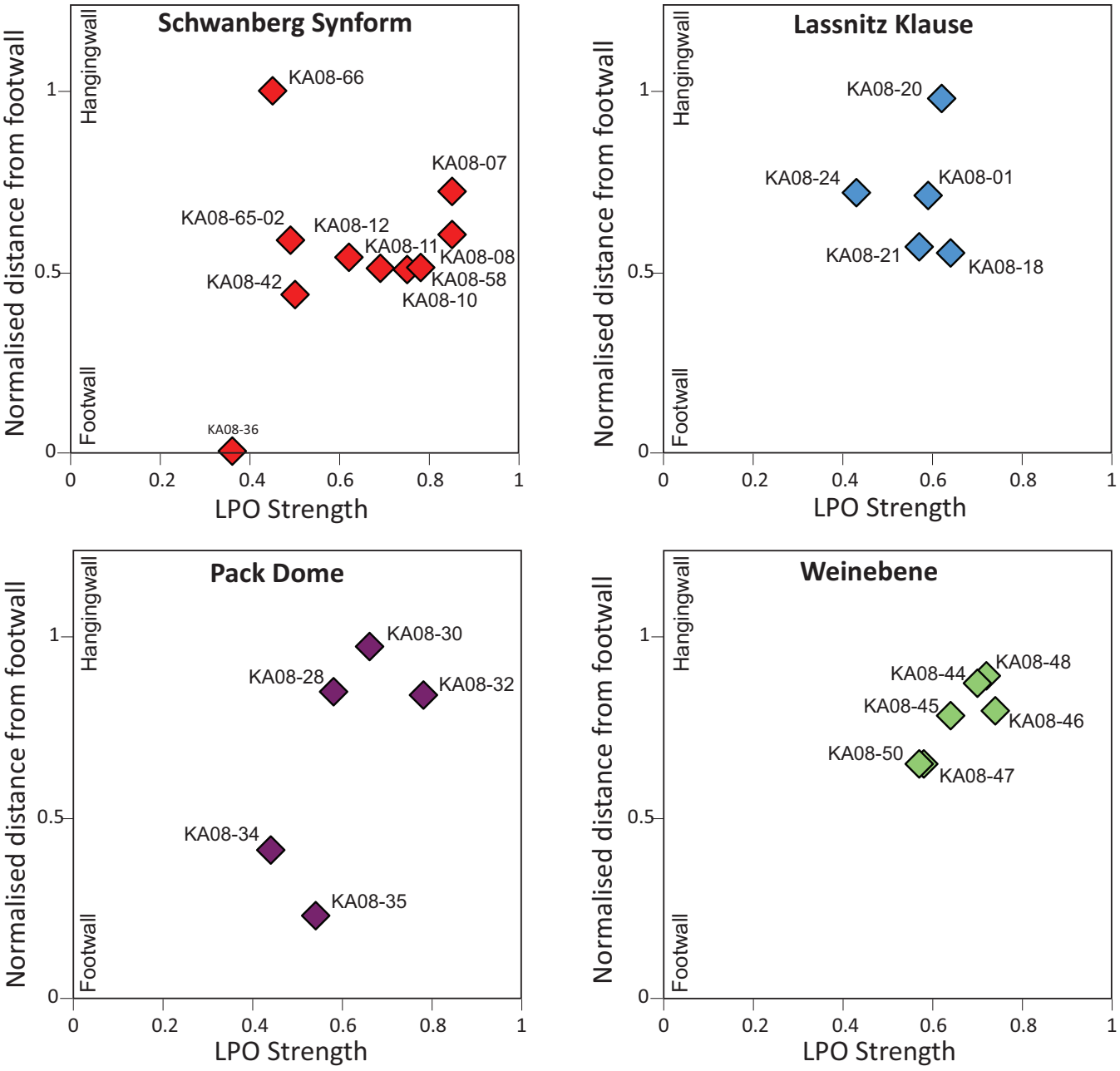

Figure 11: Graphs showing the relationship between the vertical sample location and the LPO strength (1-*R*) for all four transects.

displayed by 20 out of the 26 samples. The shear senses show no simple systematic distribution either vertically or laterally. These non-systematic shear senses found throughout the shear zone may be the result of differences in directions of shearing and in the degree of mylonitization that took place at various levels of the shear zone during its formation.

The fabrics found in this study are dominated by non-coaxial deformation, commonly with a component of constriction; no evidence for flattening was observed. No correlation was found between LPO strength and the sample's vertical position within the shear zone. Likewise, no correlation was found between the *Pn* and *Gn* values for any of the samples and their placements vertically or horizontally within the shear zone. Nevertheless, the variation of shear sense is consistent with both the microstructural data of Kurz et al. (2002) and the tectonic model of Schorn and Stüwe (2016) and therefore supports their interpretation.

6. Conclusion

Shear sense and strain geometry as recorded by quartz LPOs display no simple systematic distribution with respect to the vertical or horizontal positions of samples within the Plattengneis shear zone (Fig. 12). Deformation temperatures inferred from the LPOs do reveal north-south systematics and correlate well with the thermal

gradient inferred by Tenczer and Stüwe (2003). The four vertical transects across the shear zone exhibit a modest range of temperatures and varying strains, suggesting the shear zone may have undergone different activity and movement at different vertical levels.

The observations, measurements and inferences from this study indicate that deformation of the Plattengneis occurred at medium to high temperatures (~500 °C to 700 °C) in an environment that is largely, but not exclusively top-to-the-north non-coaxial deformation. Top-to-the-south shear sense is evident locally but does not occur in systematic positions within the shear zone. Top-to-the-north kinematics is consistent with hypotheses for the origin of the Plattengneis during the Eoalpine event via thrust-related kinematics associated with nappe emplacement (Krohe, 1987), but we suggest that it is more intuitive to think of the documented shear sense in terms of "bottom-to-the-south" as it is well known that this shear zone is the principal deformation horizon during south-directed subduction (Stüwe and Schuster, 2010; Schorn and Stüwe, 2016).

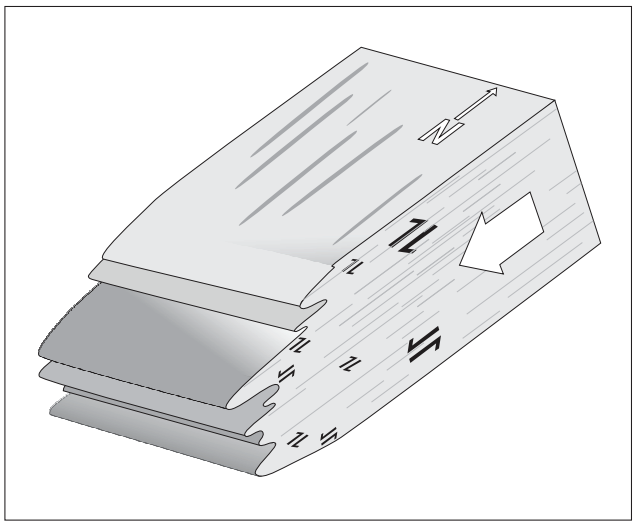

Figure 12: Cartoon showing the inferred overall shear sense of the Plattengneis with predominantly top-to-the-north (bottom-to-the-south) shear sense and some shear in the other direction so that it is not unlike an asymmetric isoclinal shear-fold. The inclined nature of the block indicated the 45° south-dip position of the shear zone at the time of deformation as inferred from the metamorphic field gradient.

Figure 12 illustrates this by way of a cartoon. With the largely "bottom-to-the-south" but also "bottom-to-the-north" shear senses, the cartoon is consistent with the model shown in Figure 2d (in particular the small inset in the left panel) confirming the model of Schorn and Stüwe (2016) and shear zone geometries as described by Passchier and Platt (2017). The subsidiary, but nonetheless evident, top-to-the-south shear sense indicators are also consistent with the model of Schorn and Stüwe (2016). The model also implies that the Plankogel detachment is indeed best interpreted as the southern continuation of the Plattengneis shear zone with the detachment being located in a position where the extraction of the central core of the shear zone is more complete.

Acknowledgements

We are grateful to Eric Kelly for his valuable assistance during field work and sample collection, and to Sharon Mosher and Robert Reed for providing technical discussion of the work and reviews of the manuscript in its original thesis format. Anna Rogowitz and Conny Roffeis are thanked for their critical reviews that significantly improved the manuscript and the handling editor Hugo Ortner is thanked for his meticulous checking of errors. The Geology Foundation of the Jackson School of Geosciences at the University of Texas at Austin provided funding for field work and analytical fees.

References

Barth N., Hacker B., Seward G.E., Walsh E., Young D., Johnston S., 2010. Strain within ultrahigh-pressure western gneiss region of Norway recorded by quartz CPOs. Continental Tectonics and Mountain Building: The Legacy of Peach and Horne. Geological Society, London, Special Publications, 335/1, 661–678. https://doi.org/10.1144/SP335.27

Eberlei T., Johnson T.E., White R.W., Roffeis C., Stüwe K., 2014. Thermobarometric constraints on pressure variations across the Plattengneiss shear zone of the Eastern Alps: implications for exhumation models during Eoalpine subduction. Journal of Metamorphic Geology, 32, 227–244. https://doi.org/10.1111/jmg.12069

Ehlers K., Stüwe K., Powell R., Sandiford M., Frank W., 1994. Thermometrically inferred cooling rates from the Plattengneis, Koralm region, Eastern Alps. Earth and Planetary Science Letters, 125/1–4, 307–321. https://doi.org/10.1016/0012-821X(94)90223-2

Flügel H.W., Neubauer F.R., 1984. Geologische Karte der Steiermark 1:20 0000, Geologische Bundesanstalt, Wien.

Froitzheim N., Pleuger J., Roller S., Nagel T.J., 2003. Exhumation of high- and ultrahigh- pressure metamorphic rocks by slab extraction. Geology, 31, 925–928. https://doi.org/10.1130/G19748.1

Gorokhovich Y., Voustianiouk A., 2006. Accuracy assessment of the processed SRTM-based elevation data by CGIAR using field data from USA and Thailand and its relation to the terrain characteristics. Remote Sensing of Environment, 104, 409–415. https://doi.org/10.1016/j.rse.2006.05.012

Haüy R.J., 1822. Traite de Mineralogie, 2nd edn. Bachelier, Paris.

Herg A., Stüwe K., 2018. Tectonic interpretation of the metamorphic field gradient south of the Koralpe in the Eastern Alps. Austrian Journal of Earth Sciences, 111/2, 155–170. https://doi.org/10.17738/ajes.2018.0010

Hirth G., Tullis J., 1992. Dislocation creep regimes in quartz aggregates. Journal of Structural Geology, 14/2, 145–159. https://doi.org/10.1016/0191-8141(92)90053-Y

Hoinkes G., Koller F., Rantitsch G., Dachs E., Höck V., Neubauer F., Schuster R., 1999. Alpine metamorphism of the Eastern Alps. Schweizerische Mineralogische und Petrographische Mitteilungen, 79, 155–181. https://dx.doi.org/10.5169/seals-60203

Krohe A., 1987. Kinematics of Cretaceous nappe tectonics in the Austroalpine basement of the Koralpe region (eastern Austria). Tectonophysics, 136/3–4, 171–196. https://doi.org/10.1016/0040-1951(87)90024-2

Kurz W., Fritz H., Tenczer V., Unzog W., 2002. Tectonometamorphic evolution of the Koralm Complex (eastern Alps): constraints from microstructures and textures of the 'Plattengneis' shear zone. Jour-

nal of Structural Geology, 24/12, 1957–1970. https://doi.org/10.1016/S0191-8141(02)00008-1

Kurz W., Froitzheim N., 2010. The exhumation of Eclogite-Facies metamorphic rocks – a review of models confronted with examples from the Alps. International Geology Review, 44/12, 1163–1164. https://doi.org/10.2747/0020-6814.44.12.1163

Lajaunie C., Courrioux G., Manuel L., 1997. Foliation fields and 3D cartography in geology: principles of a method based on potential interpolation. Mathematical Geology, 29/4, 571–584. https://doi.org/10.1007/BF02775087

Mainprice D., 2005. Pfch5 [Computer Software].

Miladinova I., Froitzheim N., Nagel T.J., Janak M., Fonseca R.O.C., Sprung P., Münker C., 2021. Constraining the process of intracontinental subduction in the Austroalpine Nappes: Implications from petrology and Lu-Hf geochronology of eclogites. Journal of Metamorphic Geology, 40, 423–456. https://doi.org/10.1111/jmg.12634

Passchier, C.W., Platt, J.P., 2017. Shear zone junctions: Of zippers and freeways. Journal of Structural Geology, 95, 188–202. https://doi.org/10.1016/j.jsg.2016.10.010

Passchier C., Trouw R., 2005. Microtectonics, 2nd ed. Springer, Germany. 105–108. https://doi.org/10.1007/3-540-29359-0

Putz M., Stüwe K., Jessell M., Calcagno, P., 2006. Three-dimensional model and late stage warping of the Plattengneis shear zone in the Eastern Alps. Tectonophysics, 412/1–2, 87–103. https://doi.org/10.1016/j.tecto.2005.10.003

Schorn S., Stüwe K., 2016. The Plankogel detachment of the Eastern Alps: petrological evidence for an orogen-scale extraction fault. Journal of Metamorphic Geology, 34/2, 147–166. https://doi.org/10.1111/jmg.12176

Stipp M., Stünitz H., Heilbronner R., Schmid S., 2002. The eastern Tonale fault zone: a 'natural laboratory' for crystal plastic deformation of quartz over a temperature range from 250 to 700 °C. Journal of Structural Geology, 24/12, 1861–1884. https://doi.org/10.1016/S0191-8141(02)00035-4

Stüwe K., Schuster R., 2010. Initiation of subduction in the Alps: Continent or ocean? Geology, 38/2, 175–178. https://doi.org/10.1130/G30528.1

Tenczer V., Stüwe K., 2003. The metamorphic field gradient in the eclogite type locality, Koralpe region, Eastern Alps. Journal of Metamorphic Geology, 21/4, 377–393. https://doi.org/10.1046/j.1525-1314.2003.00448.x

Thöni M., Jagoutz E., 1993. Isotopic constraints for eo-Alpine high-P metamorphism in the Austroalpine nappes of the eastern Alps: bearing on Alpine orogenesis. Schweizerische Mineralogische und Petrographische Mitteilungen, 73, 177–189. http://dx.doi.org/10.5169/seals-55568

Vollmer F.W., 1990. An application of eigenvalue methods to structural domain analysis. Geological Society of America Bulletin, 102/6, 786–791. https://doi.org/10.1130/0016-7606(1990)102<0786:AAOEMT>2.3.CO;2

Received: 30.10.2024
Accepted: 10.5.2025
Editorial Handling: Hugo Ortner